Dispersion of surface-modified, aggregated, fumed silica in polymer nanocomposites ⒡

Kabir Rishi (ID), Lahari Pallerla (ID), Gregory Beaucage (ID), and Anh Tang

COLLECTIONS

Paper published as part of the special topic on Polymer-Grafted Nanoparticles
Note: This paper is part of the Special Topic on Polymer-Grafted Nanoparticles.

Ⓕ   This paper was selected as Featured

View Online   Export Citation   CrossMark

ARTICLES YOU MAY BE INTERESTED IN

In situ XPS spectroscopic study of thermal stability of W/Ni bilayer Ohmic contact to n-type 4H-SiC
Journal of Applied Physics **127**, 174501 (2020); https://doi.org/10.1063/5.0002560

Janus nanoparticle synthesis: Overview, recent developments, and applications
Journal of Applied Physics **127**, 170902 (2020); https://doi.org/10.1063/5.0003329

Influence of casting substrate on bulk morphology and vanadium ion transport in ionomer nanocomposites
Journal of Applied Physics **127**, 174701 (2020); https://doi.org/10.1063/1.5144204

Dispersion of surface-modified, aggregated, fumed silica in polymer nanocomposites Ⓕ

Kabir Rishi, Ⓘ Lahari Pallerla, Ⓘ Gregory Beaucage,[a)] Ⓘ and Anh Tang

AFFILIATIONS

Chemical and Materials Engineering, University of Cincinnati, Cincinnati, Ohio 45221, USA

Note: This paper is part of the Special Topic on Polymer-Grafted Nanoparticles.
[a)]**Author to whom correspondence should be addressed:** gbeaucage@gmail.com

ABSTRACT

Surface modification of model silica to enhance compatibility in nanocomposites has been widely studied. In addition to model spherical silica, several authors have investigated the impact of surface conditions on compatibility in commercial aggregated carbon black and silica. In this paper, dispersion is investigated for a series of nanocomposites produced from commercially modified fumed silica mixed with styrene butadiene rubber, polystyrene, and polydimethylsiloxane. Surface modification includes variation in surface hydroxyl content, siloxane, and silane treatment. Qualitatively, hydroxyl groups on the silica surface are considered incompatible with non-polar polymers, while methyl groups are compatible with oleophilic polymers. X-ray scattering was used to analyze the filler aggregate structure before and after dispersion, and the second virial coefficient was used to quantify nanodispersion. The content of surface moieties was determined from Fourier-transform infrared spectroscopy. It is observed that modified silica can display mean field or specific interactions as reflected by the presence of a correlation peak in x-ray scattering. For systems with specific interactions, a critical ordering concentration is observed related to the free energy change for structuring. A van der Waals model was used to model the second virial coefficient as a function of accumulated strain, yielding the excluded volume and an energetic term. The excluded volume could be predicted from the structural information, and the bound polymer layer was directly related to the surface methyl content, whereas the energetic term was found to synergistically depend on both the methyl and hydroxyl surface content.

INTRODUCTION

Dispersion of molecules occurs by thermal diffusion, while dispersion of macroscopic particles is related to kinetic mixing reflected by the accumulated strain. Nanoparticle dispersion can have some aspects of both of these dispersion mechanisms. Mixing of aggregated nanoparticles in high polymer melts is mostly governed by kinetics, while solution mixing or compounding in low molecular weight polymers can more strongly involve aspects of thermal dispersion. At times, dispersion can involve a complex sequence of events such as the emergence of structural hierarchies during drying. Kinetically mixed polymer nanocomposites can also develop complex multi-hierarchies associated with the top–down impact of mechanical mixing, which more easily disperses larger structures.[1]

Thermal dispersion of aggregated nanoparticles is enhanced by compatibility between the filler and the matrix such as in inkjet inks modified with nonionic surfactants.[2,3] Compatibility in kinetically dispersed systems is more complex since, in many cases, it is desired to develop a macroscopic filler network requiring incompatibility such as in reinforced elastomers.[1] Incompatible filler particles seek to separate from the dispersion, but kinetic mixing locks in a dispersed state. The degree of incompatibility between the filler and the matrix can be manipulated by the introduction of favorable polymer–filler interactions or attractive interactions between filler aggregates. For instance, surface charges lead to short-range repulsion between filler particles on the nano-scale and might lead to incompatibility with nonpolar polymers.[4]

An important aspect of polymer nanocomposites is the emergence of micrometer-scale network structures responsible for many of the mechanical and optical advantages of these systems.[1] It is desirable to control these micrometer-scale network structures through the manipulation of nanoscale dispersion using surface modification and surface charges. Structural emergence in reinforced polymers can also be impacted by processing and primary

particle size, filler aggregate size, and aggregate branch topology and convolution.

In many industrial and research environments, quantification of dispersion in polymer–filler nanocomposites remains largely empirical. Direct imaging techniques such as transmission electron microscopy coupled with counting algorithms are often used for the quantification of dispersion, despite limitations on the sampling size and data interpretation from 2D projections of 3D structures.[5] As an alternative, combined small-angle and ultra small-angle x-ray scattering offers 3D structural information over multiple size scales and needs no special procedures for sample preparation. In x-ray and neutron scattering, nanoscale data are averaged over macroscopic dimensions. For industrial nanofillers, a structural hierarchy arises during particle synthesis, wherein the primary particles fuse together into aggregates which form micrometer-scale agglomerates during handling. With dispersion in high shear mixers, the filler agglomerates fracture and disperse into their base nano-scale, ramified, mass-fractal aggregates.[6] Percolation and filler–filler interactions lead to new emergent structures at larger length scales.[1,4]

The emergence of multi-hierarchical structure can be studied using small-angle x-ray scattering. The scattered intensity, $I(q) = \phi V \langle \Delta \rho \rangle^2 P(q) S(q)$, depends on the form factor, $P(q)$, the interparticle structure factor, $S(q)$, the particle volume, V, the overall filler volume fraction, ϕ, and the scattering contrast between the filler and the matrix, $\langle \Delta \rho \rangle^2$. Under dilute conditions, $S(q) = 1$ and the above expression reduces to

$$\frac{I_0(q)}{\phi_0} = V \langle \Delta \rho \rangle^2 P(q). \quad (1)$$

For spherical particles, $P(q) = \left[9\{\sin(qR) - (qR)\cos(qR)\}^2 \right]/(qR)^6$ is the square of the spherical amplitude function, where q is the reciprocal space vector and R is the sphere radius. Many academic studies of dispersion involve model systems composed of spherical colloidal silica particles with variable surface treatments, wherein the form factor for spherical particles is valid.[7] However, industrially relevant products often display a complex multi-level hierarchical, nano- to macro-scale structure. These common hierarchical industrial fillers typically display three structural levels comprised of the primary particle (level 1), aggregates of primary particles (level 2), and agglomerates of aggregates (level 3).[6,8] To account for these multi-scale structural hierarchies, the dilute reduced scattering intensity in Eq. (1) can be determined from the Unified Scattering Function[9–11] such that

$$\frac{I_0(q)}{\phi_0} = \sum_{i=1}^{n} \left[G_i \exp\left(\frac{-q^2 R_{g,i}^2}{3} \right) + B_i (q_i^*)^{-P_i} \exp\left(\frac{-q^2 R_{g,i-1}^2}{3} \right) \right], \quad (2)$$

where "i" is the structural level, G_i and B_i are the Guinier and Porod pre-factors that account for the particle volume, V, respectively, and the scattering contrast, $\langle \Delta \rho \rangle^2$; the radius of gyration, $R_{g,i}$, specifies the size of each structural level in the hierarchy; the power-law exponent, P_i, specifies the morphology of each structural level and is generally 4 for solid three-dimensional moieties with

no surface roughness, whereas it varies between 1 and <3 for mass-fractal objects. Additionally, $q_i^* = q \left[\mathrm{erf}\left(\frac{kqR_{g,i}}{\sqrt{6}} \right) \right]^{-3}$, wherein "erf" is the error function and k equals 1 for three-dimensional structures and approximately 1.06 ± 0.005 for mass-fractal structures.[9]

The dispersion of a colloidal system can be quantified with the second virial coefficient, A_2, from a virial expansion of the osmotic pressure.[12–14] The virial expansion is used to describe the impact of interactions between colloidal particles on the osmotic pressure.[15] In previous studies, x-ray scattering has been employed to quantify the pseudo-second order virial coefficient, A_2, which can be used to describe the dispersion of filler aggregates in a polymer melt.[8,16,17] Although polymer–filler blends have not been considered traditional colloids, there is precedence to use a virial expansion of osmotic pressure in viscous mixtures, where kinetic dipsersion is governed by the accumulated strain. The dependence of particle dispersion on temperature in thermally dispersed colloidal systems[18] is akin to the dependence of dispersion on the accumulated strain imparted to the polymer–filler nanocomposite. Processing conditions such as mixing time, shear rate, and material properties such as matrix viscosity[16,17] contribute to the accumulated strain and the dispersion of fillers. Dispersion is also mitigated by the filler–polymer compatibility and filler–filler interactions.

Scattering can ascertain filler–filler interactions and the effects due to polymer type and viscosity, particle size, and structure, particle concentration and processing history.[1,4,8,16,17,19–21] An obvious modification of a filler involves surface treatment. For silica fillers, a major factor influencing dispersion is the presence of hydroxyl functional groups that enhance hydrophilicity due to surface charges. These surface charges lead to short range repulsion between aggregates in precipitated silica. Reactive hydroxyl groups can be used for surface modification through hydrolysis-condensation reactions leading to new surface functionality or to grafted low molecular weight oligomeric chains chemically similar or identical to the matrix polymer.

Filler–polymer and filler–filler interactions depend on the polymer chemistry as well as the surface functionality of the filler. Bahl and Jana[22] reported on composites of lignosulfonates, a byproduct of the paper industry, in styrene-butadiene rubber (SBR). Polar surface functional groups on the lignin are incompatible with nonpolar SBR. Bahl and Jana[22] modified lignosulfonates with cyclohexylamine to enhance compatibility, which led to increased strength of the composites. Additionally, enhanced compatibility resulted in the formation of smaller particles as opposed to large randomly shaped structures.

Leblanc[23] investigated carbon black (CB) and silica nanocomposites comparing surface chemistry. The surface of carbon black may contain many functional groups but reactions involving oxygen complexes do not necessarily lead to strong rubber–carbon black interactions. However, the large quantities of siloxane and silanol groups on the surface of silica cause considerable hydrogen bonding that leads to poorer dispersibility compared to carbon black according to Leblanc.[23]

Wang et al.[24–26] linked differences in the surface chemistry of silica and carbon black to different components of the surface energy in polar and non-polar environments. It was observed that polar/basic groups were attracted to silica surfaces and less polar/

alkylene groups were attracted to the polymer matrix, thereby increasing affinity with the hydrocarbon polymer. A polar component of the surface energy was indicative of enhanced filler–filler interactions in silica that led to the formation of a more developed filler network. Additionally, modification of the silica surface was suggested to enhance the affinity between silica and polymer in order to minimize filler networking and to better balance dynamic properties. McEwan and Green previously studied PDMS-grafted silica particles with varying graft length and particle size and also quantified the interparticle interaction potential via rheology.[27]

Specific vs mean-field interactions in polymer nanocomposites

Particle–particle interactions can be specific, such as with surface charge repulsion in precipitated silica/polybutadiene rubber nanocomposites; or mean-field such as with neutral or compatibilized particle surfaces, for instance, carbon black (CB) in polystyrene–polybutadiene rubber. In scattering, systems with specific interactions display a correlation peak as modeled by the Ornstein–Zernike equation, while mean field systems display structural screening as modeled by the random phase approximation (RPA).[4]

A comparison of the concentration reduced scattered intensity above and below the overlap concentration, ϕ_0, is used to quantify the structure factor in the semi-dilute regime, $\phi \gg \phi_0$,

$$S(q) = \frac{I(q)/\phi}{I_o(q)/\phi_0}. \tag{3}$$

For mean-field systems, such as CB/SBR, the interactions can be modeled using the random phase approximation,

$$S(q) = \frac{1}{1 + \left\{ \phi v \left(\frac{I_0(q)}{\phi_0} \right) \right\}}, \tag{4}$$

where v is proportional to A_2 as described by Vogtt et al.,[21] Jin et al.,[8] and McGlasson et al.[4] In the limit of q approaching 0, $I_0(q)/\phi_0$, as described by Eq. (2), reduces to $G_2 + G_1$, the sum of the Guinier pre-factors for the first two structure levels such that the structure factor at low-q approaches

$$S(0) = \frac{1}{1 + \{\phi v(G_2 + G_1)\}}. \tag{5}$$

Thus, the second virial coefficient, A_2, can be ascertained from the Unified Fit to the dilute curve, $\frac{I_0(q)}{\phi_0}$, and the structure factors, $S(q)$, for all concentrations prior to global percolation, which results in a micrometer-scale network or clusters.

For fillers displaying specific interactions due to surface charges, such as precipitated silica, the reduced scattering intensity, $I(q)/\phi$, displays a correlation peak in the low-q regime.[8] The correlation peak is dependent on the processing history and filler–surface interactions that lead to the packing of domains with varying correlation lengths. McGlasson et al. have recently proposed a method to extract the structural details for such systems accounting for varying accumulated strain across different sample

positions and strong filler Coulombic repulsions.[4] To account for domains with different correlation lengths, ξ, a log-normal distribution of correlation distances was proposed to modify the Born–Green approximation[28] such that

$$S(q, \xi) = \int_0^\infty P(\xi) \left[\frac{1}{1 + p\theta(q, \xi)} \right] d\xi. \tag{6}$$

Where $P(\xi) = \frac{1}{\sqrt{2\pi}\xi\sigma} \exp\left(\left[-\{\ln(\xi/m)\}^2 \right]/2\sigma^2 \right)$ gives a log-normal distribution for correlation lengths with geometric mean, $m = \langle \xi \rangle \exp\left(\frac{-\sigma^2}{2}\right)$ and where σ is the geometric standard deviation. Here, $\theta(q, \xi) = \left[3\{\sin(q\xi) - (q\xi)\cos(q\xi)\} \right]/(q\xi)^3$ is the scattering amplitude function for a sphere reflecting aggregates roughly arranged in a spherical correlation shell and p, the packing factor, reflects the extent of organization of the aggregates within this shell.[28,29] $\langle \xi \rangle$ is the mean correlation distance between particles for the domains. Large p indicates better organization with $p = 0$ reflecting a random distribution. For perfect spheres in an FCC/HCP arrangement, p has a maximum value of 5.92. For irregularly shaped particles, for instance, rods or sheets, p can have values much larger than 5.92 reflecting a higher packing density. Larger values of p lead to a sharper correlation peak.

In the limit of q approaching 0, $\theta(0, \xi) = 1$ in Eq. (6). The integral of the probability distribution function, Eq. (6), over all values of ξ equals 1. Consequently, the structure factor at $q = 0$ from Eq. (6) is directly linked to the average aggregate packing factor, p,

$$S(0, \xi) = \frac{1}{1 + p}. \tag{7}$$

Comparing Eqs. (5) and (7), it can be seen that

$$v = \frac{p}{\phi(G_2 + G_1)} = \frac{p}{\phi z G_1}. \tag{8}$$

Equation (8) relates the screening parameter, v, from the mean-field approach to the specific interaction model that accounts for correlations via the packing factor, p, and the average number of primary particles in an aggregate, $z = \left(\frac{G_2}{G_1} \right) + 1$.[21,30] Both p and v reflect particulate organization but are independent of size-scale, which is described by $\langle \xi \rangle$ in both correlated and mean-field systems.[3] For both mean-field and specific interaction systems, v is a measure of the binary filler-interactions and is related to the second virial coefficient, A_2 measured in mol cm^3/g,[2,8,21]

$$A_2 = \frac{v \langle \Delta\rho \rangle^2}{2N_A \rho^2}, \tag{9}$$

where $\langle \Delta\rho \rangle^2$ is the squared difference in the scattering length density between the nanofiller and the nanocomposite matrix or the scattering contrast; N_A is Avogadro's number; and ρ is the filler density. The units of A_2 can be converted into a more familiar cm^3/aggregate by multiplying with $\frac{M^2}{N_A}$. Here, $M = \rho N_A z V_1$ is the

overall mass of an aggregate such that zV_1 represents the average aggregate contour volume.

A_2 is a direct, quantitative measure of the dispersion with larger values indicating better dispersion. Negative A_2 indicates phase segregation and $A_2 = 0$ is a critical value. Understanding the dependencies of A_2 in different polymer–filler systems is important to developing predictive techniques for the control of structural emergence in polymer–filler systems. A_2 can be used to calculate binary filler interaction potentials for coarse-grained computer simulations of complex multi-level hierarchical filler mixtures. Furthermore, the technique proposed here is not limited to any specific blend of polymers and fillers and offers the potential to be extended to a wide-range of polymer–filler systems. Control over this complex multi-hierarchical structure can be achieved through the manipulation of filler–polymer interactions such as by varying the silanol surface density, by chemically tailoring the surface, and by grafting low molecular weight polymers. It is expected that these modifications can control dispersion and the associated emergent multi-hierarchy. From the mesh size and packing of an emergent network of aggregates, the state of dispersion and the interaction potential for coarse-grain simulations can be determined.

Many commercial polymer nanocomposites involve the dispersion of aggregated nanoparticles such as silica, titania, carbon black, organic pigments, and some flame retardants and other additives. In many of these systems, a structure is built-up from nanoparticles to micrometer-scale networks through a multi-hierarchical structure. Tuning of these complex structures is typically done with simple surface chemistry, modification of processing conditions, and use of different polymer binders and matrices of variable chemical composition and molecular weight. In this study, we have examined some commercial systems limiting the study to a series of modified fumed silicas blended with three widely studied and commercially interesting polymers.

EXPERIMENTAL

Sample preparation

Three polymer matrices were used: polystyrene–polybutadiene rubber (SBR), polystyrene (PS), and polydimethylsiloxane (PDMS). SBR has been widely used for elastomer studies, and PS is useful for the broad dynamic mechanical spectrum that is available on a conventional instrument and PDMS matches the surface grafted chains on some of the commercial silicas mentioned below. These polymers were mixed with commercially available Aerosil˚ fumed silicas provided by Evonik Corporation (2 Turner Place, Piscataway, NJ 08854, USA) listed in Table I. Filler–polymer compatibility stems from the inherent chemical structure of the matrix and the surface functionalities on the filler. For example, polar groups such as surface hydroxyl on silica in a non-polar polymer such as SBR render the system incompatible, whereas surface methyl groups induced by treatment with hexamethyldisilazane (HMDS) in the same non-polar SBR make the system compatible.

Commercially available SBR with 24% vinyl, and 38% styrene content and a Mooney viscosity of 80 M.U. (ML1 + 4 at 100 °C) was mixed with chemically incompatible (Si 200 and Si 200HV) and compatible (Si 8200 and Si 9200) fumed silica nanofillers in a 50 g Brabender mixer with a Banbury style mixing geometry. A constant rotor speed of 60 rpm was applied for 12 min at 125 °C. The

temperature within the mixing chamber varied between 120 and 130 °C controlled by an air stream and cartridge heaters. During mixing, the SBR was added to the mixer followed by an antioxidant and filler. Antioxidant [N-(1,3-dimethylbutyl)-N'-phenyl-1,4-phenylenediamine] or 6PPD was provided by TCI America. Following the addition of all ingredients, mixing proceeded for 12 min. SBR-based nanocomposites were prepared with filler volume fractions, ϕ, ranging from 0.0044 to 0.14. These samples are similar to our previously reported samples in terms of mixing history and elastomer matrix.[16,17]

In addition to SBR, incompatible (Si 150, Si 200, and Si 200HV) and compatible (Si 972 and Si 974) fumed silica fillers were mixed with PS in a continuous vertical single-screw microtruder from Randcastle Extrusion Systems. Edistir˚ N3982 PS with a melt flow index of 25 g/10 min and a MW of about 125 kDa was supplied by Eni-Versalis S.p.A, Piazza Boldrini, 1-20097 San Donato Milanese (MI), Italy. The temperature of the feed, compression, and metering zones were set to 230 °C, and the die was maintained at 180 °C. A mixture of fumed silica nanofiller and polymer pellets were fed through the hopper, and the samples were extruded at a fixed screw speed of 5 rpm with a residence time of 12 min. Polystyrene-based nanocomposites were prepared with filler volume fractions (ϕ) ranging from 0.0049 to 0.06. The processing conditions and matrix polymer for the PS samples mimic those prepared by Hassinger et al.[31]

Finally, methyl-terminated PDMS with a molecular weight of ~500 g/mol purchased from Gelest was mixed at room temperature with incompatible (Si 200) and compatible (Si 202 and Si 208) fumed silica fillers listed in Table I using a vortex mixer from Fisher Scientific for 30 s at 3200 rpm. The MW of the PDMS was chosen such that the polymer and graft-PDMS chain lengths are approximately equal. After mixing, the nanocomposite was allowed to settle to remove air bubbles prior to measurement. PDMS-based nanocomposites were prepared with filler volume fractions, ϕ, ranging from 0.0041 to 0.07.

Ultra-small angle x-ray scattering (USAXS)

For scattering studies, 1 mm thick specimens were pressed on a platen for 10 min at ~100 °C for SBR and ~130 °C for PS nanocomposites. The SBR samples were further mounted in flat metallic washers, whereas the PS samples were used as free-standing films for USAXS measurements. PDMS samples were loaded into thin glass capillaries with an ID of about 1 mm.

USAXS measurements were performed at beamline 9ID-C, which is designed and operated by Jan Ilavsky at the X-ray Science Division at the Advanced Photon Source (APS) at the Argonne National Laboratory.[32,33] Scattered intensity from the specimens was recorded in the range of $0.0001 \, \text{Å}^{-1} \leq q \leq 0.1 \, \text{Å}^{-1}$ using an incident radiation of $\lambda = 0.5904 \, \text{Å}$. The USAXS data sets were reduced, corrected for background scattering from the polymer, and subsequently de-smeared to account for slit smearing. Absolute intensities were scaled by the filler volume fraction. The Nika and Irena packages for Igor Pro˚ were employed to reduce and de-smear the data sets.[34,35]

Oscillatory rheology

Rheological measurements were performed using a parallel plate geometry on a Discovery HR-2 rheometer by TA instruments.

To determine the zero shear-rate viscosity of SBR and PS under operating conditions, circular disks of about 4 mm thickness with a diameter of 20 mm were prepared by pressing the samples at 120 °C for 10 min between heated platens. Frequency scans at a constant strain amplitude of 0.1% were performed at different temperatures (25 °C to 200 °C for SBR and 150 °C to 200 °C for PS in steps of 25 °C) under nitrogen. These data were subsequently time-temperature superposed using the Williams-Landel-Ferry (WLF) equation to generate master curves over a wide frequency range. The reference temperature for the SBR master curve was 125 °C, whereas it was 200 °C for PS. These reference temperatures were chosen based on the processing conditions.

Fourier transform infrared spectroscopy

FTIR spectra from pristine fumed silica powders, listed in Table I, were obtained on a Nicolet 6700 FT-IR spectrometer. IR transmittance from the samples was converted into absorbance using OMNIC® FTIR software. For a quantitative estimate of the different functional groups on the surface, the ratio of areas under the peak was considered. For fumed silica, Si 200, the silanol density on the surface was reported to be $2.8/nm^2$ through careful thermogravimetric analysis by Mueller et al.[36] This value was used to estimate the number of siloxane (Si–O–Si) groups per volume of silica. Under the assumption that the number of siloxane groups per volume remains constant, the content of all other functional groups on the surface/bulk can be estimated. The content of the key functional groups is listed in Table II in the results section.

IR analysis of silica

Figure 1 shows the FTIR absorbance spectra of the different fumed silica powders. For all grades of fumed silica, strong sharp peaks lying between $400–530 \, cm^{-1}$, $750–900 \, cm^{-1}$, and $950–1300 \, cm^{-1}$ are associated with the deformation vibration of O–Si–O, symmetric stretching vibration and antisymmetric stretching vibration of Si–O–Si, respectively.[37–40] It is observed that all grades show a broad peak between 3000 and $3600 \, cm^{-1}$, as shown in the inset of Fig. 1(a), which is associated with hydroxyl (−OH) functionalities on the surface.[37,41] Note that the slight dip at $3750 \, cm^{-1}$ is an instrumental artifact. The broad peaks are more

pronounced for Si 150, Si 200, and Si 200HV fumed silicas indicating a larger surface hydroxyl content as opposed to the surface-modified fumed silicas. All surface-modified hydrophobic silicas show a distinct peak between 2950 and $3000 \, cm^{-1}$ as shown in the inset of Fig. 1(b), which is attributed to the methyl (−CH₃) functionalities.[41] The peak height correlates with the surface carbon content. This peak is large for Si 202, Si 208, and Si 8200 indicating the presence of longer hydrocarbon chains on the surface or a larger grafting density of carbon functional groups. Notice that this peak is very small for Si 972, Si 974, and Si 9200, and it is completely absent for the hydrophilic silicas, Si 150, Si 200, and Si 200HV.

Table II lists the surface hydroxyl and methyl functional group contents for the different fumed silicas. For Aerosil® Si 200, the hydroxyl surface content was determined to be $2.8/nm^2$ via thermogravimetric analysis.[36] Since the siloxane (Si–O–Si) peak in the region of $950–1300 \, cm^{-1}$ in Fig. 1 results from the bulk of the fumed silica, this value can be used to normalize the surface content of the particles knowing the surface area to volume ratio $\left(\frac{S}{V}\right)$ from scattering. A ratio of the area under the FTIR peaks can then be used as a measure of the surface content of each functional group, x, such that

$$\frac{A_x}{A_{SiO}} = \frac{N_x}{N_{SiO}}\left(\frac{S}{V}\right) = \frac{N_x}{N_{SiO}}\left(\frac{6}{d_p}\right). \quad (10)$$

Here, A_x is the area under the broad hydroxyl peak and sharp methyl peaks for when $x = OH$ and $x = CH_3$ respectively, whereas A_{SiO} is the area under the sharp siloxane peak. N_x is the number of hydroxyl groups/nm² for $x = OH$ or number of methyl groups/nm² for $x = CH_3$, whereas N_{SiO} represents the number of siloxane groups/nm³. For Aerosil Si 200, the hydroxyl

TABLE I. Aerosil fumed silica grades and surface functionalities.

Raw material	Raw material	Surface treatment
Aerosil® fumed silica	Si 150	Hydroxyl groups with varying silanol density
	Si 200	
	Si 200HV	
	Si 202	Grafted with low-MW PDMS
	Si 208	
	Si 972	Treated with dimethyldichlorosilane (DDS)
	Si 974	
	Si 8200	Treated with hexamethyldisilazane (HMDS)
	Si 9200	Proprietary modification of Si 974

TABLE II. Surface-hydroxyl (N_{OH}) and surface-methyl (N_{CH_3}) content for different Aerosil fumed silica grades.

Silica grade	N_{OH} [a] (surface hydroxyl/nm²)	N_{CH_3} [a] (surface methyl/nm²)	Predominant surface functional groups [b]
Si 150	2.80 (±0.001)	0	−OH
Si 200	2.80 (±0.003)	0	
Si 200HV	2.41 (±0.002)	0	
Si 202	0.25 (±0.001)	0.553 (±0.001)	$-[(CH_3)_2Si-O]_n$
Si 208	0.025 (±0.007)	0.904 (±0.001)	−
Si 972	0.44 (±0.002)	0.070 (±0.001)	$(CH_3)_2Si-O$
Si 974	0.54 (±0.001)	0.031 (±0.001)	
Si 8200	1.16 (±0.001)	0.17 (±0.01)	$-Si(CH_3)_3$
Si 9200	0.85 (±0.002)	0.078 (±0.001)	$(CH_3)_2Si-O$

[a]Obtained from the FTIR peak analysis for the surface functional groups, $x = OH$ and $x = CH_3$ and by considering a fixed number of siloxane groups/nm³ for each fumed silica sample. The error in surface content results from the propagated error in the surface area to volume ratio $\left(\frac{S}{V}\right)$ from the measured statistical error in scattering for each fumed silica powder using Eq. (10).
[b]From product specifications in Table I.
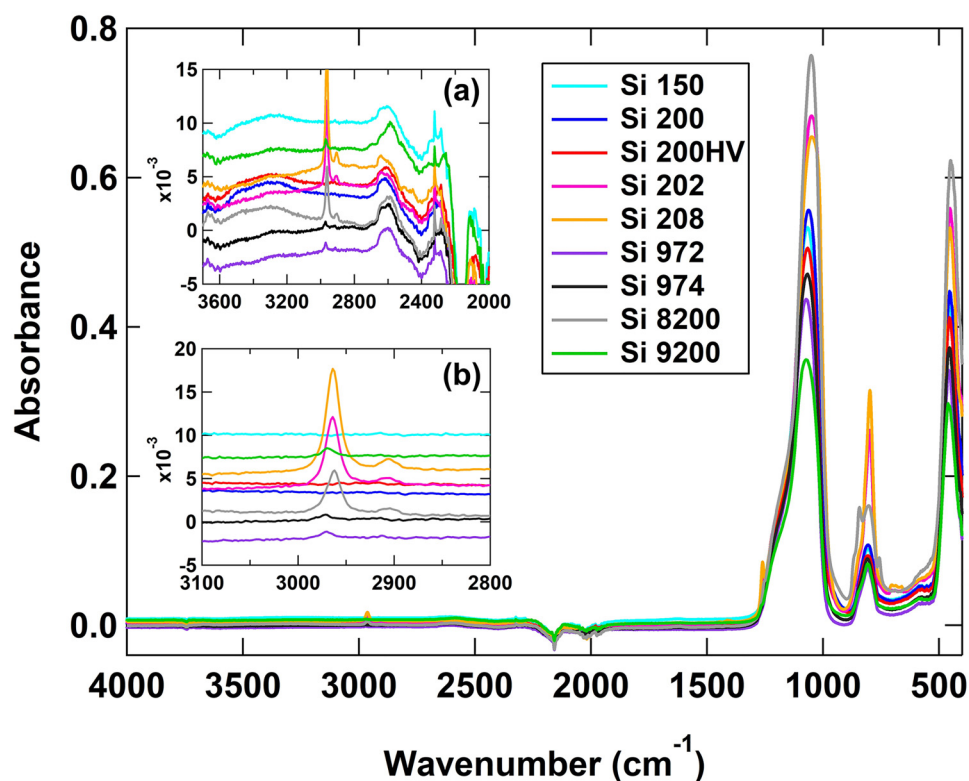
FIG. 1. FTIR spectra for different fumed silica grades; inset figure (a) showing the broad -OH peaks in the 3000–3600 cm^{-1} range for all fumed silicas; inset figure (b) showing the sharp -CH$_3$ peak in the 2950–3000 cm^{-1} range for surface modified silicas (Si 202, Si 208, Si 972, Si 974, Si 8200, and Si 9200) but absent for the unmodified fumed silicas (Si 150, Si 200, and Si 200HV). Note that the slight dip at 3750 cm^{-1} is an instrumental artifact.

surface content was determined to be 2.8/nm^2 via thermogravimetric analysis.[36] This measure of N_{OH} was used to ascertain N_{SiO} from the peak areas in the Si 200 FTIR spectra. N_{SiO} is a constant for determining N_{OH} and N_{CH_3} for the remaining fumed silica powders listed in Table II.

From Table II, it can be seen that fumed silicas with PDMS-grafted on the surface (Si 202 and Si 208) have a larger surface content of methyl groups as opposed to the fumed silicas treated with HMDS (Si 8200) and dimethyldichlorosilane (Si 972, Si 974, and Si 9200), since the number of methyl groups on the grafted PDMS chain with $n \sim 7$–8 is larger. Additionally, Si 8200 has a higher methyl content than Si 972, Si 974, and Si 9200. The inherent differences in chemical structure of the graft species listed in Table I agree with the computed methyl content in Table II. Figure 2 compares the number of surface methyl groups/nm^2 (N_{CH_3}) for treated fumed silicas with the surface carbon content estimated via carrier gas hot extraction analysis in an elemental analyzer as listed in the product specifications. In this method, a weighed sample is combusted in a ceramic crucible at high temperatures in the presence of oxygen. The quantity of effused carbon dioxide is measured by infrared detectors. The ratio of the measured quantity of CO_2 to the initial sample weight is expressed as the percentage carbon content on the surface of the silica. The amount of carbon on the surface was determined by normalizing
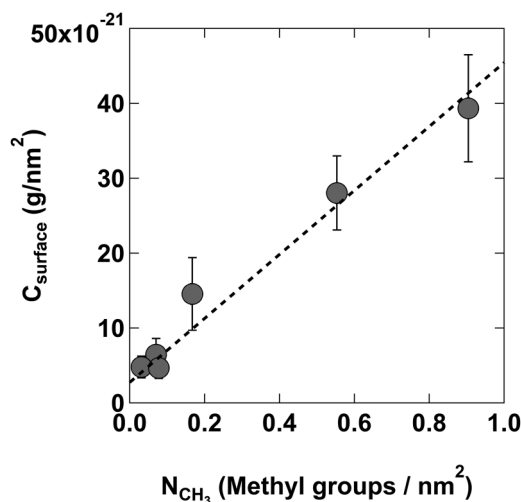
FIG. 2. Comparison of $C_{surface}$ determined from the percentage carbon content in the product specifications and normalized by the surface area to mass ratio of treated fumed silicas to the number of methyl groups per nm^2 (N_{CH_3}) from IR analysis. The dashed line indicates a linear relationship. The small positive intercept corresponds to the error in measurement.
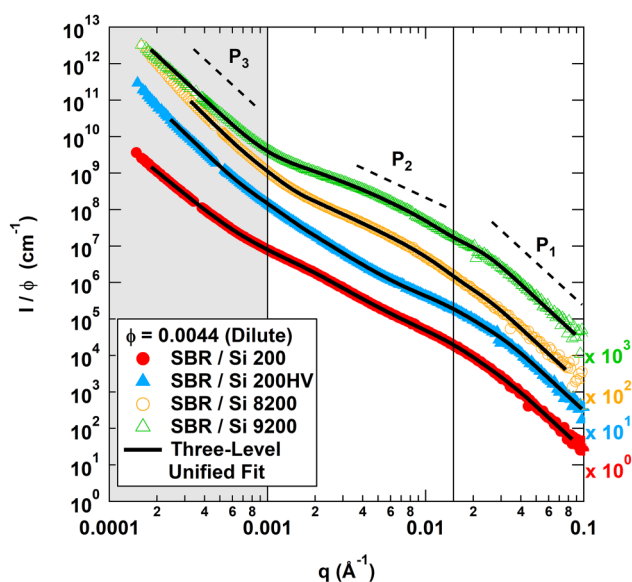
FIG. 3. A log–log plot of the reduced scattered intensity, $\frac{I_0(q)}{\phi_0}$ ($\phi_0 = 0.0044$) vs the scattering vector, q for incompatible fillers (Si 200 and Si 200HV) and compatible fillers (Si 8200 and Si 9200) mixed with styrene-butadiene rubber. Note that the curves are scaled by decades for clarity. Each curve was fit to the three-level Unified Function [Eq. (2)] indicated by the solid black lines. The three regions have distinct power-law slopes, $P_1 = -4$, $-1 \leq P_2 < -3$, and $-3 < P_3 \leq -4$ corresponding to the primary particle (smallest), mass fractal aggregates, and agglomerates (largest). The fit parameters for the first two structural levels are listed in Table S1 in the supplementary material.

the percentage carbon content by the surface area to mass ratio, $C_{surface} = (\%C)/(S/(V\rho)) = (\%C)/\big(6/(\rho d_p)\big)$. A strong correlation (dashed line) supports the estimate of the methyl content on the surface of the fumed silicas as listed in Table II, using FTIR.

RESULTS

Small-angle x-ray scattering

Figure 3 shows the scattered intensity, $\frac{I_0(q)}{\phi_0}$ vs q for dilute samples ($\phi_0 = 0.0044$) of SBR nanocomposites. The dilute curves are used to measure the filler structure in the absence of significant correlations. Note that some of the curves were scaled by a decade for the purpose of distinguishing between curves, although the fits were performed on unscaled curves. Each curve was fit to the Unified Function, Eq. (2), indicated by the solid black line. The fit parameters are listed in Table S1 in the supplementary material.

Figure 3 shows that three structural levels can be observed, each marked by a power-law slope and a corresponding Guinier knee to the left of the power-law. In the reciprocal space, each structural level represents a substructure of the filler hierarchy such that small q values contain information of the largest size-scale structures. At $q < 0.001$ Å^{-1}, a power-law slope of between $-3 < P_3 < -4$ is attributed to surface scattering from micrometer-scale agglomerates of fumed silica particles. The larger the slope, the smoother the surface

with the surface fractal dimension being given by $d_s = 6 - P_3$. It is to be noted that the Guinier knee for this region, though absent in USAXS, could be observed in static light scattering or in ultra-small angle neutron scattering measurements.[42]

In the intermediate q range, $0.001 < q < 0.03$ Å^{-1}, a power-law slope ranging from $-1 \leq P_2 < -3$ indicates mass-fractal scattering from fumed silica aggregates that make up the micrometer-scale agglomerates. From the corresponding Guinier knee in this region, the aggregate size ($R_{g,2}$) was determined. The $q = 0$ intercept for the Guinier region yields the weight average degree of aggregation. The highest q region, $q > 0.03$ Å^{-1}, displays surface scattering from the smallest hierarchical component. This region is also characterized by a weak Guinier knee related to the radius of gyration of the primary particles, $R_{g,1}$, which are solid three-dimensional entities with a power-law slope of $P_1 = -4$ indicating smooth surfaces. USAXS plots for different fumed silica grades in polystyrene ($\phi_0 = 0.0049$) and PDMS ($\phi_0 = 0.0041$) and the corresponding Unified Fit parameters are available in Figs. S1 and S2 and Table S1 in the supplementary material. Additionally, Table S2 in the supplementary material lists the fit parameters for the different filler powders of Table I prior to dispersion. The structural information of the neat fillers serves as a reference for comparison with fillers in their mixed state, under the assumption that the aggregate structure is invariant with concentration.

Effect of processing on size and topology of aggregates

The fit parameters from Tables S1 and S2 in the supplementary material were used to compute additional structural and topological information[10,11] about the filler hierarchies before and after dispersion as listed in Table III and Table S3 in the supplementary material. The weight average number of primary particles within an aggregate or the degree of aggregation, $z = \left(\frac{G_2}{G_1}\right) + 1$, was determined from the ratio of the Guinier pre-factors.[21,30] The Sauter mean diameter for the primary particles (the diameter of a sphere with the same surface to volume ratio), $d_p = 6\left(\frac{S}{V}\right)^{-1} = 6\left(\frac{\pi B_1}{Q_1}\right)^{-1}$ where Q_1 is the scattering invariant.[11,43] The aggregate end-to-end distance, $R_{eted} = d_p(z)^{1/d_f}$ is a measure of the aggregate size using $d_f = -P_2$, the mass-fractal dimension of the aggregate, whereas the polydispersity of primary particles is determined from the prefactors in the Unified Fit, $PDI = G_1 R_{g,1}^4/(1.62 B_1)$.[11] Other topological parameters such as the aggregate branch content, ϕ_{br}, the aggregate conductive path dimension, d_{min}, and aggregate connectivity dimension, c, are also listed in Table III.[10] In Table III, the derived topological parameters for both dispersed and non-dispersed fillers from scattering are used to simulate similar aggregates using a code provided by Mulderig et al.[20] In Table III, $R = R_{eted}/d_p$ is a dimensionless aggregate size obtained from the simulated structures. The images of simulated aggregates of Si 200 before and after dispersion in SBR, PS, and PDMS are shown in Fig. 4. From Table III, it can be observed that for the same filler, for example, Si 200 which is incompatible with the polymers (SBR, PS, and PDMS), a considerable difference in aggregate topology exists before and after dispersion. For example, the primary particle size, d_p for the hydroxyl-surfaced Si 200 *decreased* when milled with PS and SBR but *increased* after

TABLE III. Aggregate topological parameters from scattering results compared with the parameters from simulated aggregates in Fig. 4 for nanocomposites before and after dispersion.

Filler/nanocomposite		d_p (nm)	R_{eted} (nm)	z	d_f	d_{min}	c	ϕ_{br}	PDI
Before dispersion									
Si 200	Scattering	12.8 (±0.07)	170 (±4)	160 (±6)	1.97 (±0.01)	1.2 (±0.1)	1.6 (±0.1)	0.84 (±0.05)	10 (±0.5)
	Simulation		R = 14	158[a]	1.9	1.3	1.5	0.79	—
Si 8200	Scattering	13 (±0.1)	160 (±5)	220 (±15)	2.17 (±0.01)	1.4 (±0.1)	1.6 (±0.1)	0.86 (±0.09)	10 (±1)
	Simulation		R = 13	223[a]	1.9	1.2	1.6	0.86	—
After dispersion									
SBR/Si 200	Scattering	11.4 (±0.05)	150 (±1)	560 (±10)	2.45 (±0.03)	2.1 (±0.1)	1.2 (±0.1)	0.56 (±0.02)	9 (±1)
	Simulation		R = 18	550[a]	2.2	1.5	1.4	0.85	—
PS/Si 200	Scattering	12.2 (±0.05)	105 (±3)	240 (±8)	2.55 (±0.07)	2.1 (±0.1)	1.2 (±0.1)	0.66 (±0.05)	9 (±3)
	Simulation		R = 13	240[a]	2.1	1.7	1.3	0.70	—
PDMS/Si 200	Scattering	14.2 (±0.06)	195 (±3)	120 (±3)	1.82 (±0.03)	1.1 (±0.1)	1.6 (±0.1)	0.83 (±0.04)	15 (±2)
	Simulation		R = 17	118[a]	1.7	1.1	1.5	0.78	—
SBR/Si 8200	Scattering	13.7 (±0.04)	390 (±3)	800 (±10)	2.0 (±0.01)	2.0 (±0.1)	1.0 (±0.1)	0 (±0.06)	12 (±1)
	Simulation		R = 29	800[a]	2.0	1.7	1.2	0.70	—

[a]Input for simulation.

mixing with PDMS. The average number of primary particles per aggregate, z, showed the opposite trend, indicating that smaller primaries led to a larger degree of aggregation, z. The end-to-end distance, R_{eted} for Si 200 reduced on mixing with SBR, while it increased for HMDS treated Si 8200. On the contrary, the fractal dimension of Si 200 and Si 8200 showed the opposite trend after mixing with SBR, indicating changes in the branch content coupled with changes in z. These results indicate that changes in the multihierarchical structure on milling under different surface treatments are complex. Hashimoto *et al.* hypothesized that the anisotropy in an aggregate shape may reflect a difference in binary filler interactions.[6]

$R_{g,1}$ is expressed as the square root of higher order moments in size, $\langle R^8 \rangle / \langle R^6 \rangle$ and is not a good measure of the primary particle size. For instance, break up of one large cluster that was shifting the high order moments can drop $R_{g,1}$ dramatically without changing the median particle size. Consequently, the Sauter mean diameter, d_p expressed as the ratio of the third to second moment of size

Incompatible systems

Compatible system

Unmodified Si

Si 200 (a)

SBR / Si 200 (c)

PS / Si 200 (b)

PDMS / Si 200 (d)

200 nm

200 nm

200 nm

200 nm

Modified Si

Si 8200 (e)

SBR / Si 8200 (f)

400 nm

400 nm
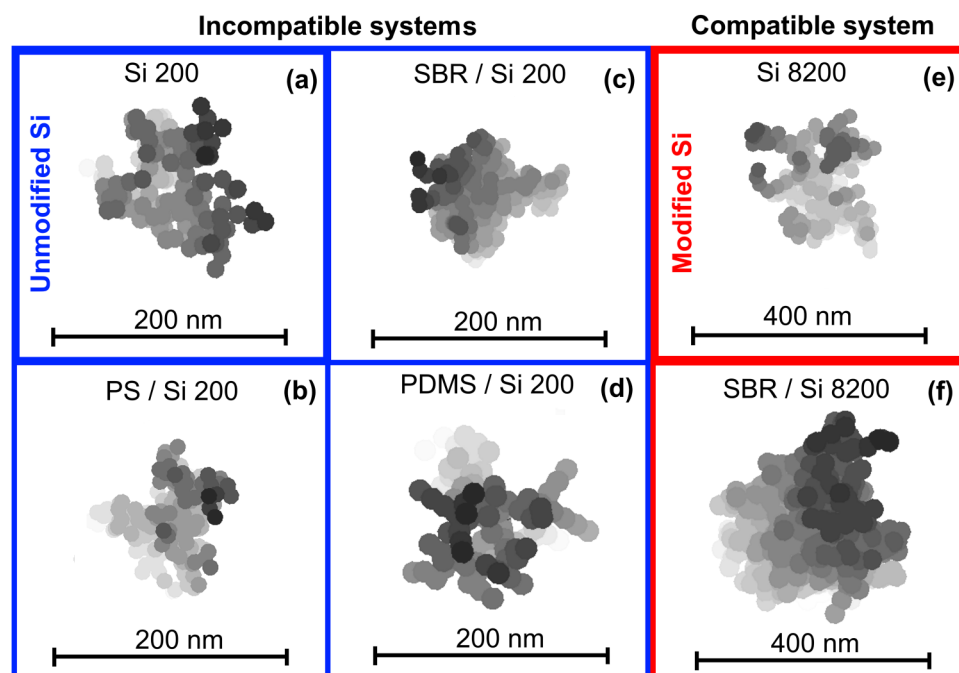
FIG. 4. Simulated aggregates of Si 200 and Si 8200 before [(a) and (e)] and after [(b)–(d), and (f)] dispersion in various polymer matrices generated from the code provided by Mulderig *et al.*[20] The calculated aggregate topological parameters approximately agree with the scattering result in Table III. Stereographs and rotational videos of the 3D structures are available in the supplementary material.
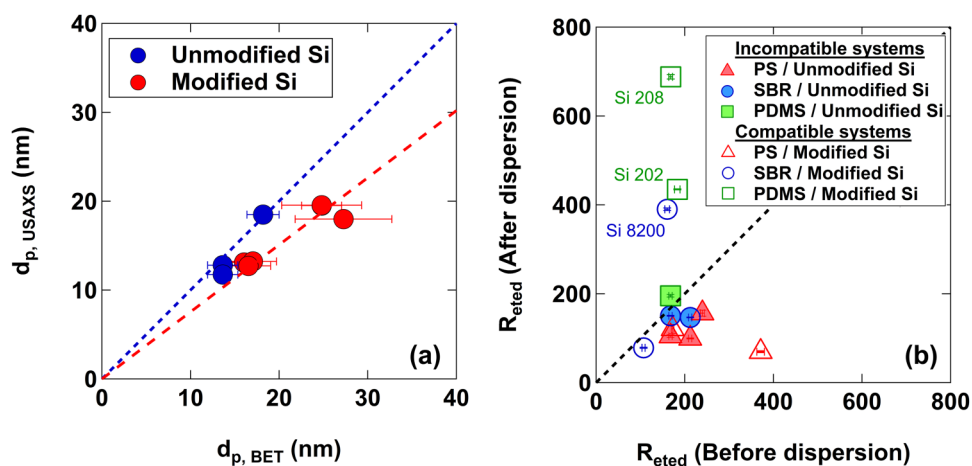
FIG. 5. (a) A plot comparing the Sauter mean diameter from fits to the scattering curves, $d_{p,USAXS}$ before dispersion to the primary particle diameter from the specific surface areas listed in the product specifications, $d_{p,SSA}$ for various fumed silica grades considering a density of 2.2 g/cm^3. The red dashed line in (a) indicates a lower apparent filler density for modified silica; (b) A plot comparing the aggregate end-to-end distance, R_{eted} for fumed silicas before and after dispersion in different polymer matrices. The dashed black line in (b) indicates that the aggregate end to end distance before and after dispersion remains unchanged.

is a better measure. Changes in $R_{g,1}$ and d_p after processing in Tables S1 and S2 (refer to the supplementary material) and Tables III and S3 (refer to the supplementary material) respectively, can be attributed to the particle polydispersity expressed as *PDI*. For all filler–polymer combinations, a reduction in $R_{g,1}$ and d_p within error after processing is associated with a lower particle polydispersity as expected for most dispersive mixing processes, with the exception of Si 8200 in SBR and Si 200, Si 202 and Si 208 in PDMS. For Si 8200 in SBR and Si 200 in PDMS, a marginal increase in $R_{g,1}$ and d_p after processing and an increased particle polydispersity indicates that the particles clump on mixing. Although, an increase in polydispersity after mixing indicates nanoclustering for Si 202 and Si 208 in PDMS the mean size, d_p drops in both. $R_{g,1}$ for Si 202 increases, whereas it decreases for Si 208 in PDMS indicating that the effects of different processing methodologies for the three classes of nanocomposites are complex.

Figure 5(a) contrasts the primary particle Sauter mean diameter obtained from the scattering of filler powders with that from gas absorption/BET specific surface area (*SSA*) measurements as listed in the product specifications such that

$$d_{p,BET} = \frac{6000}{\rho\,SSA}. \qquad (11)$$

Here, the specific surface area is measured in m^2/g, and the silica density is assumed to be 2.2 g/cm^3 following Mulderig *et al.*[20] The dashed black line (upper line) in Fig. 5(a) indicates that $d_{p,USAXS} = d_{p,BET}$ for incompatible fumed silica powders, in agreement with Mulderig *et al.* However, for compatible fillers, the two values do not agree. Scattering measures both open and closed pores, while gas absorption only measures open pores. This could explain a higher specific surface area and a lower d_p for the scattering values from compatible fillers. The shift could also reflect a lower apparent density [Eq. (11)] for the compatible, polymer grafted silica aggregates due to the lower density surface grafted material since the bulk silica density was used in Eq. (11).

Figure 5(b) compares the aggregate end-to-end distance, R_{eted} of the fumed silicas before and after dispersion in the three polymer matrices (with different processing conditions) mentioned in the Experimental section. R_{eted} was chosen for comparison since it accounts for changes in d_p, z, and d_f due to processing. The dashed line in Fig. 5(b) indicates that the ratio of R_{eted} before and after dispersion is 1. In Fig. 5(b), it can be seen that for incompatible fillers (solid symbols) R_{eted} either reduces or remains constant after processing. For compatible fillers, a smaller average aggregate size for extruded polystyrene-based nanocomposites (open red triangles) indicates that the shear forces during extrusion are larger as opposed to mixing in a Brabender for SBR based nanocomposites (open blue circles). The vortex mixing procedure for low molecular weight PDMS (open green square) resulted in the largest aggregate size. Although compatible fillers (open symbols) showed a reduction when the surface methyl content was low, a considerable increase was observed for fillers with a large surface methyl content (Si 8200, Si 202, and Si 208). This is not unexpected since during processing the reduction in aggregate size is balanced by agglomeration. Based on the methyl content estimates from FTIR in Table II, Si 202 has a shorter graft density as opposed to Si 208. In the low MW methyl terminated PDMS used here, the larger graft density results in a larger R_{eted}.

Estimation of the second virial coefficient, A_2

Systems displaying mean-field interactions

Figures 6(a) and 6(b) show the reduced scattering intensity under semi-dilute filler concentration, $\frac{I(q)}{\phi}$, as a function of reciprocal scattering vector, q, plotted on the left ordinate for SBR/Si 8200 and SBR/Si 9200 nanocomposites. The corresponding structure factor, $S(q)$, from Eq. (3) for each concentration is plotted on the right ordinate. In Figs. 6(a) and 6(b), it can be seen that all $\frac{I(q)}{\phi}$ curves match the dilute curve, $\frac{I_0(q)}{\phi_0}$ (black circles), at high q indicating that the primary particle structure remains unchanged with increasing filler concentration. Thus, $S(q) = 1$ at high q. However, $\frac{I(q)}{\phi}$ diminishes in the intermediate q range for semi-dilute concentrations, which indicate the overlap of structural features at the
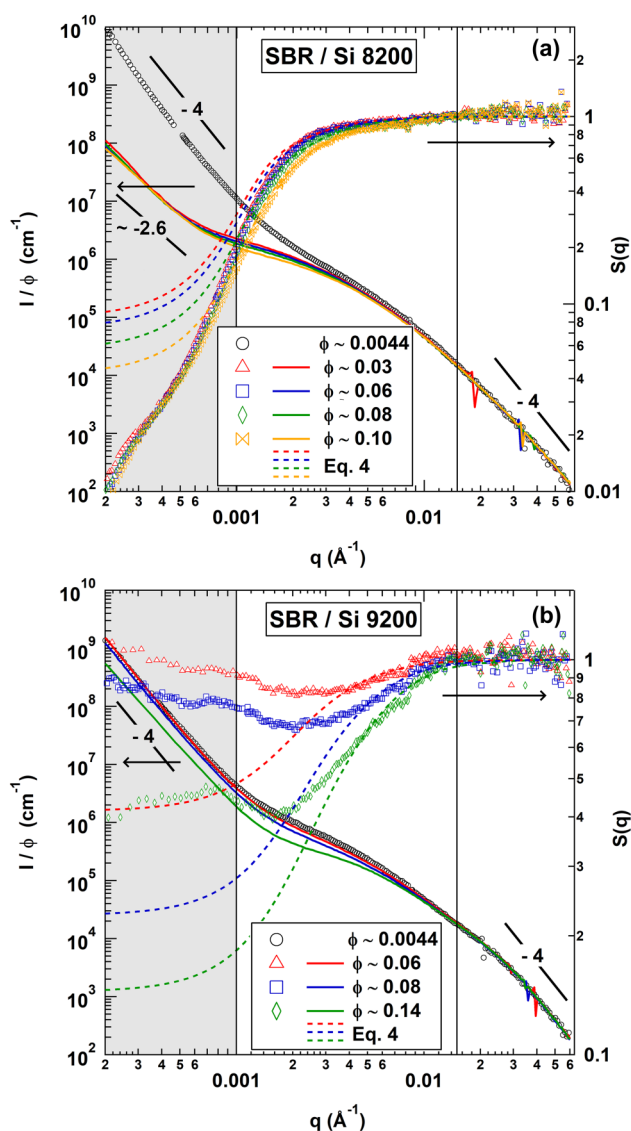
FIG. 6. Reduced scattering intensity, $\frac{I(q)}{\phi}$, read from the left axis and the structure factor, $S(q)$, read from the right axis as a function of reciprocal space vector, q for (a) SBR/Si 8200 and (b) SBR/Si 9200 at different semi-dilute filler volume fractions. The dilute reduced scattering intensity, $\frac{I_0(q)}{\phi_0}$ vs q at $\phi_0 = 0.0044$ for both fillers in (a) and (b) marked by black circles is shown for reference. $S(q)$ was obtained from $\frac{I(q)}{\phi}$ following Eq. (3). The absence of a peak in (a) and (b) indicates a mean-field behavior bereft of structural correlations. Fits to $S(q)$ in (a) and (b) using Eq. (4) are indicated by the dashed lines. The shaded region at low q deviates from the fits due to large-scale agglomerate structures and is not included in the fit model.

aggregate level leading to local percolation.[1] At low q [$q < 0.001 \, \text{Å}^{-1}$, indicated by the shaded region in Figs. 6(a) and 6(b)], the semi-dilute concentrations of Si 9200 in SBR show an approximately constant $S(q)$ since the same −4 power-law slope for

the dilute concentration is observed, although the reduced scattering intensity from the agglomerates is screened. However, a change in power law dependence to a mass-fractal power-law of −2.6 slope ($d_f = 2.6$) for Si 8200 in SBR in this same q-region indicates the formation of a large-scale filler network at all semi-dilute concentrations.

Although the surface hydroxyl content results in correlated structures, as discussed below, the difference in surface methyl content listed in Table II could perhaps be responsible for the formation of a globally percolated structure in SBR/Si 8200 ($N_{CH_3} = 0.17/\text{nm}^2$) as opposed to SBR/Si 9200 ($N_{CH_3} = 0.078/\text{nm}^2$). Similarly, with decreasing q in the low-q regime, an approximately constant $S(q)$ is observed for PS/Si 972 and PS/Si 974 [refer to Figs. S3(d) and S3(e) in the supplementary material] owing to a low surface methyl content listed in Table II. Although the agglomerate region is absent for PDMS/Si 202 and PDMS/Si 208 [refer to Figs. S4(b) and S4(c) in the supplementary material], a steep reduction in $S(q)$ with decreasing q in the low-q regime indicates that the local nano-scale percolated network extends globally on the micrometer scale. Thus, a larger surface methyl content results in global filler networking.

$S(q)$ for each concentration in Figs. 6(a) and 6(b) and Figs. S3 (d), S3(e), S4(b), and S4(c) in the supplementary material was fit to Eq. (4) from which the screening parameter, v, was determined. This value agreed with the $q = 0$ intercept, $S(0)$, per Eq. (5). The second virial coefficient, A_2, was determined using Eq. (9). $S(0)$ is inversely related to the packing factor, p, as defined in Eq. (7) and depends on the filler concentration and the screening parameter, v, which is a measure of particle interactions.

The fits per Eq. (4) [indicated by dashed lines in Figs. 6(a) and 6(b)] at the same volume fraction, for example, $\phi = 0.06$ result in a lower $S(0)$ read from the right axis for SBR/Si 8200 (dashed blue line) in Fig. 6(a) as opposed to $S(0)$ for SBR/Si 9200 (dashed red line) in Fig. 6(b) indicating that Si 8200 aggregates pack better in SBR. This could be attributed to the larger surface hydroxyl content for Si 8200 ($N_{OH} = 1.16/\text{nm}^2$) as compared to Si 9200 ($N_{OH} = 0.85/\text{nm}^2$) in Table II. Similarly, at $\phi = 0.04$, Si 202 in PDMS with 0.25 hydroxyls/nm² [indicated by the dashed green line in Fig. S4(b) in the supplementary material] shows a better packing than Si 208 in PDMS with 0.025 hydroxyls/nm² [indicated by the dashed red line in Fig. S4(c) in the supplementary material]. Additionally, the packing for Si 972 and Si 974 in PS is comparable at $\phi \sim 0.02$ as indicated by the dashed blue line in Fig. S3(d) and dashed green line in Fig. S3(e) in the supplementary material due to comparable surface hydroxyl contents in Table II. These results indicate that the arrangement of aggregates and the second virial coefficient depend on the surface hydroxyl content, N_{OH}.

Systems with specific interactions and a critical ordering concentration (COC)

Figures 7(a) and 7(b) show the structure factors, $S(q)$ as a function of reciprocal scattering vector, q for SBR/Si 200 and SBR/Si 200HV nanocomposites at semi-dilute filler concentrations. Untreated fumed silicas such as Si 200 have a high −OH surface content and are characterized by the absence of −CH₃ functionalities on the surface. The hydroxyl groups are hydrophilic which
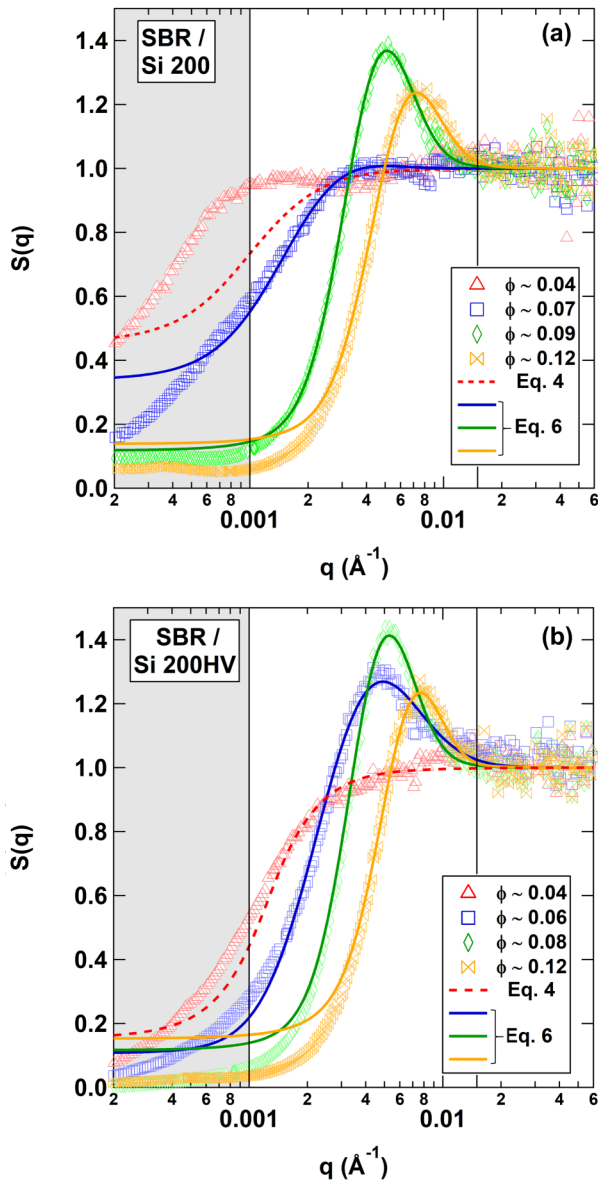
FIG. 7. A plot of the structure factor, $S(q)$, vs the reciprocal space vector, q for (a) SBR/Si 200 and (b) SBR/Si 200HV with filler volume fractions varying from $\phi \sim 0.04$ to $\phi \sim 0.12$. No peak is observed for the lowest concentration and the data is fit to Eq. (4) as indicated by the dashed red lines. A peak is observed with increasing concentrations indicating the emergence of correlated structures and the solid lines are fit per Eq. (6). Note that the peak for $\phi \sim 0.07$ indicated by the blue squares in (a) is very shallow. The shaded region at low q deviates from the fits due to large-scale agglomerate structures.

detract from their compatibility with SBR. As discussed previously, $S(q) = 1$ at high q indicates that the primary particle structure remains unchanged at all concentrations. A reduction of $S(q)$ in the intermediate q range up to low volume fractions, $\phi \sim 0.04$ indicates the overlap of structural features at the aggregate level. However, on

further increase in concentration, a peak appears in the intermediate q region indicating the emergence of correlated structures that could be attributed to a pronounced filler–filler repulsion owing to the significant surface hydroxyl content in these systems.

In Figs. 7(a) and 7(b), $S(q)$, for low volume fractions up to $\phi \sim 0.04$, was fit using the mean-field equation (4) (red dashed lines). In order to account for the emergent correlated structures at higher volume fractions, Eq. (6) was used (solid lines). The absence of a correlated peak at lower concentrations indicates that correlations between aggregates in these systems are related to the distance between aggregates, which reduces with increasing concentration. For low dielectric materials, the Debye screening length is small, $\lambda_D \sim \kappa^{1/2}$. This means that repulsive forces due to the charged aggregates are only felt at short distances or at moderate concentrations. When the average aggregate separation distance approaches λ_D, a critical ordering concentration (COC) is reached, and the system can no longer be described with a mean-field model.

The fit parameters to the solid lines in Figs. 7(a) and 7(b) indicate that the correlation distance/mesh size averaged over all domains of varying accumulated strain, $\langle \xi \rangle$, is related to the peak position for higher concentrations as shown later. Additionally, the peak width is mostly a measure of the log-normal standard deviation, σ from Eq. (6). The packing factor, p from the fits per Eq. (6) can alternatively be estimated from $S(q = 0)$, Eq. (7). The estimate of p from Eq. (6) was used to determine the screening parameter, υ from Eq. (8) which was used to determine A_2 from Eq. (9).

Figure 8 shows a cartoon of the structural rearrangement of aggregates with increasing concentration of fillers with only hydroxyl functionalities on the surface in incompatible systems such as Si 200HV in SBR. Variable strain in different locations lead to domains of different correlation lengths. At low concentrations below ϕ_{COC}, aggregates are randomly arranged and can be described with a mean-field model, whereas domains of correlation appear at higher concentrations, above a critical ordering concentration associated with the interaggregate distance/mesh size reducing below λ_D. The emergence of a correlation peak in Figs. 7(a) and 7(b) with increasing concentration seems to indicate that a free energy change on ordering, ΔG, exists analogous to the free energy change on micellization. In analogy to the critical micelle concentration, the critical ordering concentration might be given by $\phi_{COC} = \exp\left(\frac{\Delta G}{\gamma}\right)$, where the accumulated strain, γ, is used in viscous systems governed by kinetic dispersion in a similar analogy to the temperature in thermally dispersed systems since both temperature and accumulated strain favor dispersion in a similar manner. For low viscosity PDMS nanocomposites, it might be considered that both thermal and kinetic dispersion contribute so $\phi_{COC} = \exp\left(\frac{\Delta G}{\{k\gamma + RT\}}\right)$ where k is a constant that relates thermal and kinetic mixing energy.

The correlation length between aggregates is determined by the concentration, the charge on the aggregates, dielectric constant of the media, and by the local accumulated strain. The aggregates are distributed into domains distinguished by different correlation length associated with variable accumulated strain in different regions of the sample. At low concentrations, particles are separated by distances larger than the Debye screening length, λ_D, and the effect of the charged surface hydroxyls is not felt by adjacent
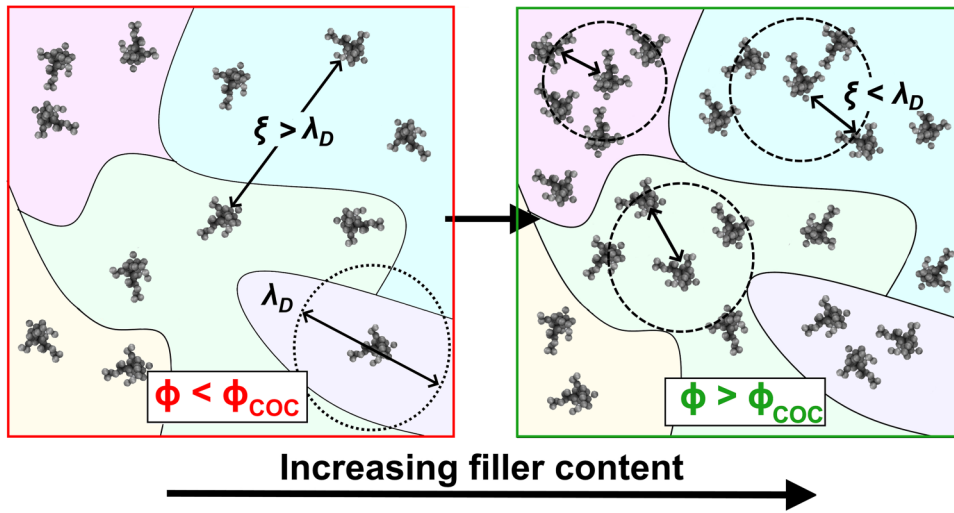
FIG. 8. A cartoon showing the critical ordering in incompatible filler-polymer systems such as Si 200/SBR with increasing filler content. The transition is marked by the emergence of a correlation peak at intermediate q in scattering above the critical ordering concentration, ϕ_{COC} that indicates the formation of domains of correlation.

aggregates within a domain resulting in a random distribution and mean-field behavior. With increased concentration, the correlation length or mesh size within the domains is reduced below λ_D such that the repulsive charges result in aggregate ordering within the domains. Different accumulated strain domains contain ordered structures with different mesh sizes, which averaged over all domains can be modeled through Eq. (6). Although incompatible fillers mixed with SBR display a correlation peak in Figs. 7(a) and 7(b), this effect was not observed when the same fillers were mixed with PS and PDMS as shown in Figs. S3(a), S3(b), S3(c), and S4(a) in the supplementary material since these systems were still below their critical ordering concentration, except PS/Si 200 which shows a broad and weak correlation peak at $\phi = 0.06$ in Fig. S3(b) in the supplementary material. The dielectric constant for PS[44] and PDMS[45] is similar, $\kappa_{PS} \sim 2.5$ and $\kappa_{PDMS} \sim 2.56$, whereas the dielectric constant for SBR, $\kappa_{SBR} \sim 6.25$.[46,47] This means that for similar particle charges the Debye screening length is about 1.58 times larger for SBR and the critical ordering concentration above which

charges lead to repulsion and ordering should be about four times lower for SBR in agreement with the observed behavior.

Figure 9(a) shows the average mesh size, $\langle \xi \rangle$ obtained from the $S(q)$ fit to Eq. (6) in Figs. 7(a) and 7(b) as a function of ϕ^{-1/d_f} for different filler concentrations. A linear dependence indicates that the mesh size scales with its fractal dimension in agreement with Mulderig et al.[19] Additionally, $\langle \xi \rangle$ from the fits was compared to the mesh size, $\langle \xi \rangle = \frac{2\pi}{q'}$, where q' corresponds to the peak position in the $S(q)$ plots. The two values are in good agreement for larger filler concentrations indicating that stronger specific interactions modeled via Eq. (6) can be reduced to a two-parameter fit. Equation (6) has three fit parameters: the mesh size averaged over all domains, $\langle \xi \rangle$; the aggregate packing, p; and the geometric standard deviation, σ. $S(q)$ as a function of q is fit using a least-squares minimization involving a numerical integration of the average mesh size, $\langle \xi \rangle$. At large concentrations, where $\langle \xi \rangle$ from the fit approximates $\langle \xi \rangle$ from the correlation peak, the two fit parameters that remain are p and σ.
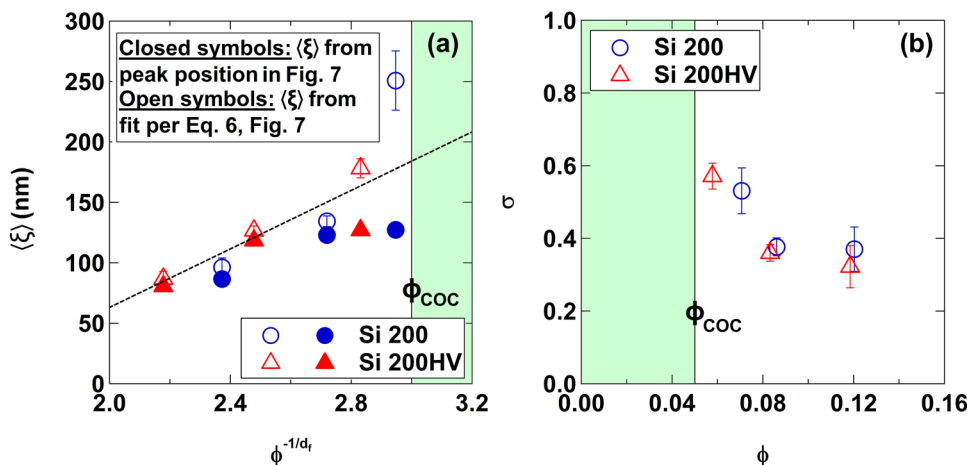
FIG. 9. (a) A plot comparing the mesh size or correlation distance to a function of filler concentration suggested by Mulderig et al.[19] The mesh size is obtained from the peak position in the $S(q)$ plots and from fits of $S(q)$ to Eq. (6) in Fig. 7; (b) a plot showing the variation in geometric standard deviation vs volume fraction filler determined from the $S(q)$ fits to Eq. (6) in Fig. 7 for Si 200 and Si 200HV in SBR. The shaded region in (a) and (b) indicates the onset of the critical ordering concentration, ϕ_{COC}, below which at low volume fractions the system displays a mean-field behavior.
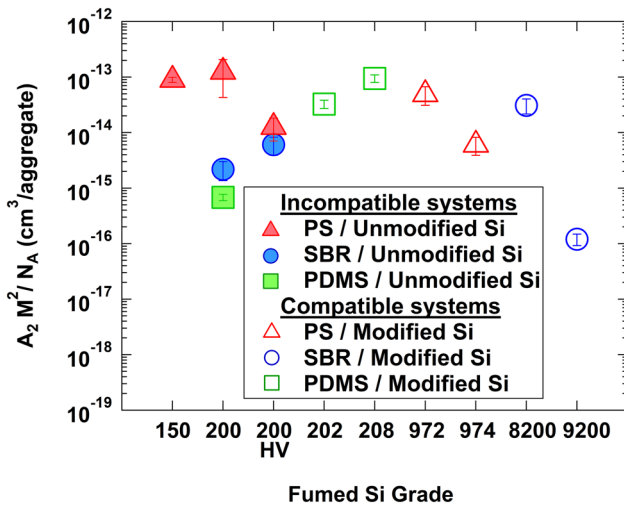
FIG. 10. A plot of A_2 normalized by $\frac{M^2}{N_A}$ for each fumed silica filler/polymer combination in this study. A larger value of normalized A_2 represents better dispersion.

Figure 9(b) shows the geometric standard deviation for the mesh size from the fit to Eq. (6), σ, as a function of the filler volume fraction. σ decreases with volume fraction for both Si 200 and Si 200HV in SBR indicating a narrower distribution of correlation lengths as the packing becomes closer and the electrostatic interactions begin to dominate over the accumulated strain distribution. The σ values for the two fillers are almost identical indicating that the distribution in accumulated strain is related to the mixer geometry and matrix viscosity. The average accumulated strain for nanocomposites processed with the same mixer geometry at a constant fill volume is a function of the mixing duration, matrix viscosity, and shear rate. Since both Si 200 and Si 200HV were mixed with SBR under the same conditions, it is hypothesized that σ is related to the average variability in accumulated strain in the processed nanocomposites. An increase in the variability in accumulated strain would lead to a larger distribution of mesh sizes.

Figure 10 shows A_2 normalized by $\frac{M^2}{N_A}$, where M represents the aggregate mass, for the fumed silica fillers in different matrices. In PS, the normalized A_2 for incompatible fillers (solid red triangles) is generally larger (better dispersion) than that for compatible fillers (open red triangles). However, in SBR and PDMS, compatible fillers (open blue circles and open green squares) disperse better, as indicated by larger A_2 values for Si 8200 in SBR, and surface grafted-PDMS on Si 202 and Si 208 in PDMS matrix. This could be attributed to an enhanced packing, p which is inversely related to $S(0)$ in Fig. S4 in the supplementary material and indicates a better distribution of Si 202 and Si 208 aggregates in PDMS. Additionally, for all three compatible fillers (Si 8200 in SBR, and Si 202 and Si 208 in a PDMS matrix), a significant increase in the degree of aggregation, z after processing, as listed in Tables III and S3 in the supplementary material, results in a larger aggregate volume, V_2, that is directly related to the normalized A_2. Both the

topological changes and the aggregate arrangement in the matrix are intimately tied to the processing history and the surface characteristics as discussed below.

If the amount of surface methyl content is chosen as a qualitative measure of compatibility in non-polar PDMS, with greater N_{CH_3} indicating better compatibility, then PDMS/Si 208 and PDMS/Si 202 (open green squares in Fig. 10) represent systems with $\frac{W_{PF}}{W_{FF}} > 1$, where W_{PF} is the work of adhesion of the filler to polymer and W_{FF} is the work of adhesion of the filler to itself as defined by Hassinger et al.[31] Concomitantly, PDMS/Si 200 (closed green square in Fig. 10) represents an incompatible system with $\frac{W_{PF}}{W_{FF}} < 1$. A larger value of A_2 for PDMS/Si 208 and PDMS/Si 202 as opposed to PDMS/Si 200 indicates that enhancing compatibility improves filler dispersion in agreement with Hassinger et al.[31] For compatible PDMS (Si 202 and Si 208) systems, the ratio of the matrix to the graft chain length is approximately 1. The variation in methyl content in Table II indicates that the graft density for Si 208 ($\sim 0.9/nm^2$) is larger than that for Si 202 ($\sim 0.55/nm^2$). Kumar et al.[48] proposed a phase diagram that relates the structural changes in polymer grafted nanocomposites to the graft density and the ratio of matrix to graft chain lengths. From the above estimates for the PDMS/Si 208 system, well-dispersed nanoparticles are expected which agrees with the larger dispersion observed for Si 208 in PDMS. Although, a connected sheet morphology for Si 202 is expected from Kumar et al.[48] this could not be verified.

Impact of surface methyl and hydroxyl content on A_2

Van der Waals expression for A_2

The dependence of the normalized A_2 on processing conditions has been modeled with a pseudo van der Waals function, where an analogy between temperature and accumulated strain is used,

$$A_2\left(\frac{M^2}{N_A}\right) = b^\star - \frac{a^\star}{\gamma}, \qquad (12)$$

where $b^\star$ is the excluded volume and $a^\star$ is proportional to the attractive energy between aggregates in the context of the accumulated strain, γ, which is proportional to strain energy, and replaces temperature or thermal energy, RT, in the usual van der Waals expression. For constant shear rate and mixing geometry, the accumulated strain, γ, is approximately proportional to the mixing time.[16,17] In Refs. 16 and 17, mixing time was varied and Eq. (12) was solved for $a^\star$ and $b^\star$. In these two references, it was consistently found that the excluded volume, $b^\star$, could be calculated from the structural parameters obtained in the dilute Unified Fit. $b^\star$ was found to reflect the contour volume of the chain aggregate, $4zV_{pp}$, where V_{pp} is the volume of a primary particle, $V_{pp} = \pi d_p^3/6$ for the neat silica and carbon black powders. In the current study, measurements at different accumulated strains were not possible so $b^\star$ was calculated from the structural parameters obtained from the dilute scattering patterns. This allowed for the determination of the energetic term, $\frac{a^\star}{\gamma}$ from the measured A_2 values.

In these elastomer nanocomposites, the calculated $b^\star$ is consistently larger compared to that of the neat powders reflecting the bound rubber layer. $\Delta b^\star = b^\star_{nanocomposite} - b^\star_{neat\ powder}$ is a measure of
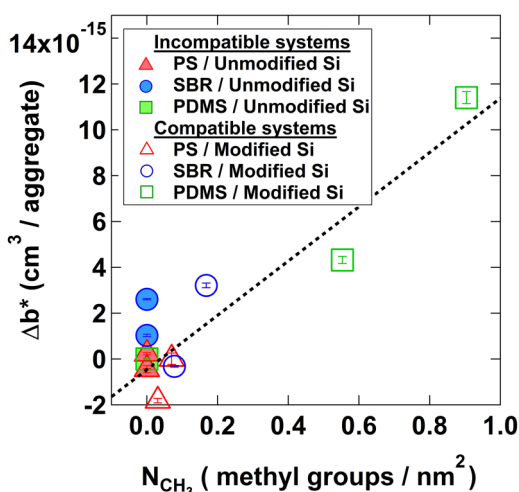
FIG. 11. A plot showing the bound polymer content (Δb^*) determined from the excluded volumes of the filler aggregates before and after dispersion as a function of surface methyl content (N_{CH_3}). The dashed line indicates that Δb^* is proportional to N_{CH_3} determined from FTIR.

the surface volume occupied by bound rubber chains and grafted chains. Figure 11 shows the bound polymer determined from the difference in excluded volumes, Δb^*, of the fumed silicas in the three polymers as a function of surface methyl content (N_{CH_3}) before and after processing. It can be seen that Δb^* increases with increasing N_{CH_3} indicating that the compatibilization of the filler with the polymer matrix positively impacts the bound rubber layer, thereby enhancing b^* after processing.

From b^*, the parameter $\frac{a^*}{\gamma}$ can be determined using the measured A_2 values in Eq. (12). γ can be estimated from the mixing time, extruder residence time, or vortexing time and an estimate of the mixing speeds for the three mixing geometries. $\gamma = N\Psi t$ was considered where N represents the mixing speed, t represents the mixing time, and Ψ accounts for the mixing geometry.[16,17] The geometry effects can be ignored if all polymers are processed on the same equipment.[16,17] For Brabender mixing of SBR nanocomposites, the twin-rotor internal mixer can be approximated using a simple Couette flow following Bousmina *et al.*[49] such that $\Psi = \left[4\pi(\beta)^{2/n}\right]/\left(n\left\{(\beta)^{2/n} - 1\right\}\right)$. Here, β is the ratio of wall to rotor diameter equal to 1.14 for the Brabender geometry in this experiment, and n is the power-law index under shear flow which was estimated to be approximately 1 for SBR by Sadhu and Bhowmick.[50] For the extrusion of PS nanocomposites, the single-screw extruder mixing geometry constant can be approximated following Hassinger *et al.*[31] as $\Psi = \frac{\pi\{d - 2H(L)\}}{H(L)}$, where d is the screw diameter and $H(L)$ is the channel depth that depends on the screw length, L. For the extruder used in this study, $d = 11.7$ mm and the channel width at the end of the metering zone, i.e., $H(343 \text{ mm}) = 1$ mm. For PDMS subject to vortex mixing, the vortex mixer was approximated by an equivalent bob-cup geometry. Considering a large cylinder gap for this geometry, $\Psi = \frac{2\pi(2R^2)}{(R^2 - r^2)}$

at the axis of rotation, where R is the cup radius and r is the radius of the bob.[51] For this experiment, $r \ll R$ was considered such that Ψ reduces to 4π.

Figure 12 shows the attractive energy, a^* described above as a function of the surface content of both hydroxy and methyl groups. Negative values of a^* indicate repulsion of aggregates, while positive values drive clustering and separation. In Fig. 12, a^* is plotted as a function of the surface concentration, $\phi_{surf} = N_{OH} + k'N_{CH_3} + k''N_{OH}N_{CH_3}$ on a log scale, where k' is a measure of the relative impact of the hydrophobic (N_{CH_3}) and hydrophilic (N_{OH}) surface functionalites. Additionally, k'' in the cross term accounts for the blocking of interactions by the two surface groups, for example, hydrocarbon chains could shield hydroxyl groups from interaction with the matrix or with other filler aggregates.

For PS, SBR, and PDMS based nanocomposites, the attractive energy term, a^*, shows a logarithmic dependence on the surface concentration of functional groups with the same functional form as $\exp\left(\frac{Energy}{kT}\right)$, with kT being replaced by C_1 or γ. This indicates that the balance between interparticle repulsions and the accumulated strain that dictates the extent of dispersion is impacted by the effect of both hydrophilic and hydrophobic surface groups.

In Fig. 12, the points for SBR, PS, and PDMS nanocomposites are distinguished by blue circles, red triangles, and green squares. These three sets of samples are fit separately since the energetics of interaction, a^*, and accumulated strain, γ, differ between the sets. k' is negative for PS but positive for SBR and PDMS. A negative value of k' indicates that the addition of methyl groups reduces the attraction between particles in the context of that polymer matrix and those processing conditions. PS shows a negative k', while SBR shows a relatively large positive k' indicating that the addition of methyl groups to the silica surface in SBR enhances aggregate attraction.

k'' reflects the impact of the addition of methyl groups on the activity of hydroxyl groups. A negative value of k'' indicates that methyl groups diminish the activity of hydroxyl groups in enhancing attraction between aggregates. A value of k'' of zero indicates no symbiotic interaction between the groups. This occurs for SBR. A positive value of k'' indicates that the the interactions of the two surface groups in the attraction of aggregates are symbiotically enhanced. For PS and PDMS, the hydroxyl and methyl groups are symbiotic.

The constant C_2 reflects the relative intensity of the impact of the two surface functional groups on aggregate interaction energy in the context of kinetically dispersed nanocomposites. Additionally, the different slopes represented by C_1 to the fits in Fig. 12 for the three polymers can be attributed to the different matrix viscosities and the overall accumulated strain due to the different mixing geomtries.

In the context of accumulated strain as an energy of dispersion, the viscosity of the matrix polymer governs the dispersibility of the nanoaggregates. That is, for the same accumulated strain, the impact on particle dispersion is smaller for higher viscosity polymers since it is more difficult to transport aggregates in a more viscous media. The matrix viscosities for SBR and PS at

Fit Function: $a^* = C_1 \ln(C_2 \phi_{surf})$
Open symbols: Compatible Si
Closed symbols: Incompatible Si

	k'
PS	-5
SBR	15.5
PDMS	5

	k''
PS	70
SBR	0
PDMS	3

	C_2
PS	0.6 (±0.1)
SBR	0.45 (±0.05)
PDMS	0.35 (±0.01)

x-axis: $\ln C_2(N_{OH} + k'N_{CH_3} + k''N_{OH}N_{CH_3})$ or $\ln(C_2\phi_{surf})$
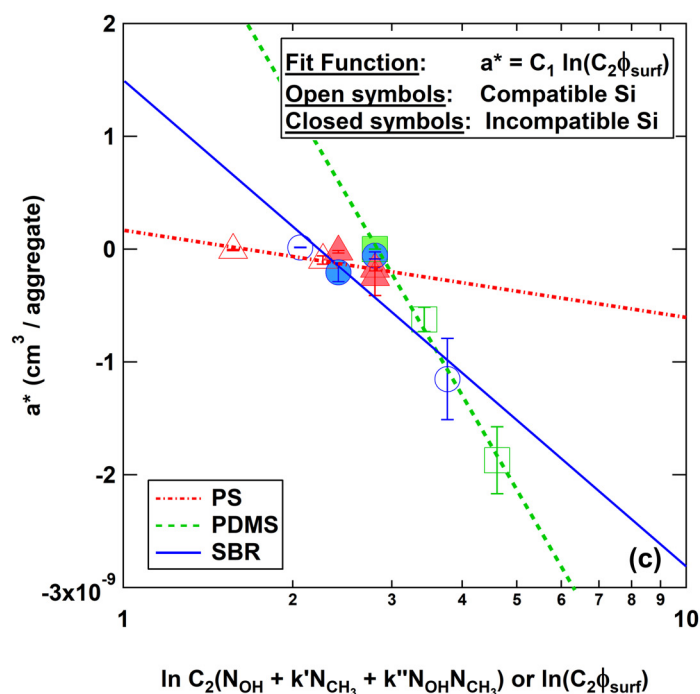
FIG. 12. A plot showing the relative impact of both hydroxy (N_{OH}) and methyl groups (N_{CH_3}) surface concentration on the attractive energy (a^*). The dashed (PDMS), solid (SBR) and dash-dotted (PS) lines are fit to $a^* = C_1 \ln(C_2 \phi_{surf})$ which has the same functional dependence as $\exp\left(\frac{Energy}{kT}\right)$ on concentration, where a^* is an attractive energy.

processing temperatures of 125 °C and 200 °C, respectively, were determined through oscillatory rheology measurements by constructing master curves based on the WLF equation. From the master curves shown in Figs. S5 and S6 in the supplementary material, the dynamic viscosity at lowest frequency was chosen as the zero shear rate viscosity ($\sim 10^4$ Pa s for PS and $\sim 10^5$ Pa s for SBR) using the Cox–Merz rule.[52] Additionally, the viscosity of PDMS at room temperature was ascertained form the product specifications (3 cSt $\sim 2.7 \times 10^{-3}$ Pa s). Figure 13 shows the slope for the a^* fits in Fig. 12 normalized by the accumulated strain, $\frac{C_1}{\gamma}$, as a function of the zero shear rate viscosities, η for all three polymers at their respective processing temperatures. A linear dependence confirms that C_1 is a measure of the total strain energy that accounts for the accumulated strain and the polymer viscosity on dispersion in the van der Waals function proposed above.

In summary, filler compatibility in non-polar polymers depends on the presence of charged-hydroxyl or neutral-methyl surface moieties. Filler interactions in conventional as well as surface-modified fumed silica aggregates display a mean field behavior below ϕ_{COC}, where the aggregates are separated by distances larger than the Debye screening length, λ_D, and the interaggregate repulsion due to surface charges is not felt by the adjacent aggregates (Fig. 14). Above ϕ_{COC}, the correlation length or mesh size reduces below λ_D such that the repulsive charges result in the emergence of correlated aggregates. ϕ_{COC} bears some resemblance to the critical micelle concentration in that it reflects a transition from disordered to ordered states in concentration. ϕ_{COC} reflects a balance between the free energy of ordering and the overall accumulated strain imparted during dispersion, which plays the role of

temperature in dispersing the filler aggregates. The interaction energy from the van der Waals expression is a synergistic result of the relative amounts of the two surface functionalities as summarized in Fig. 14.
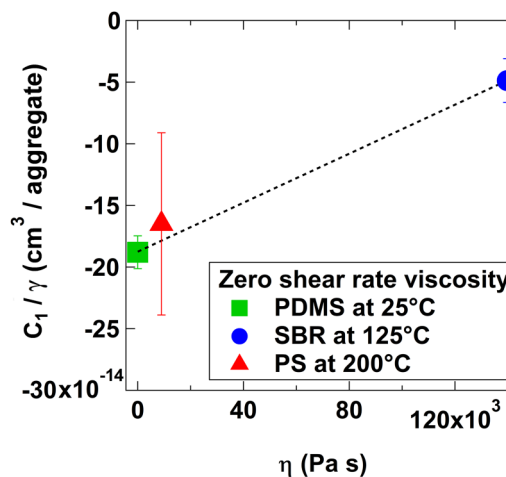
FIG. 13. A plot showing the dependence of the slope of the fits in Fig. 12 normalized by the computed accumulated strain, $\frac{C_1}{\gamma}$, on the zero shear rate matrix viscosity, η at the processing temperature. Calculations of the accumulated strain, γ, for all three mixing geometries are detailed in Table S4 in the supplementary material. The dashed line in (c) indicates a linear dependence.
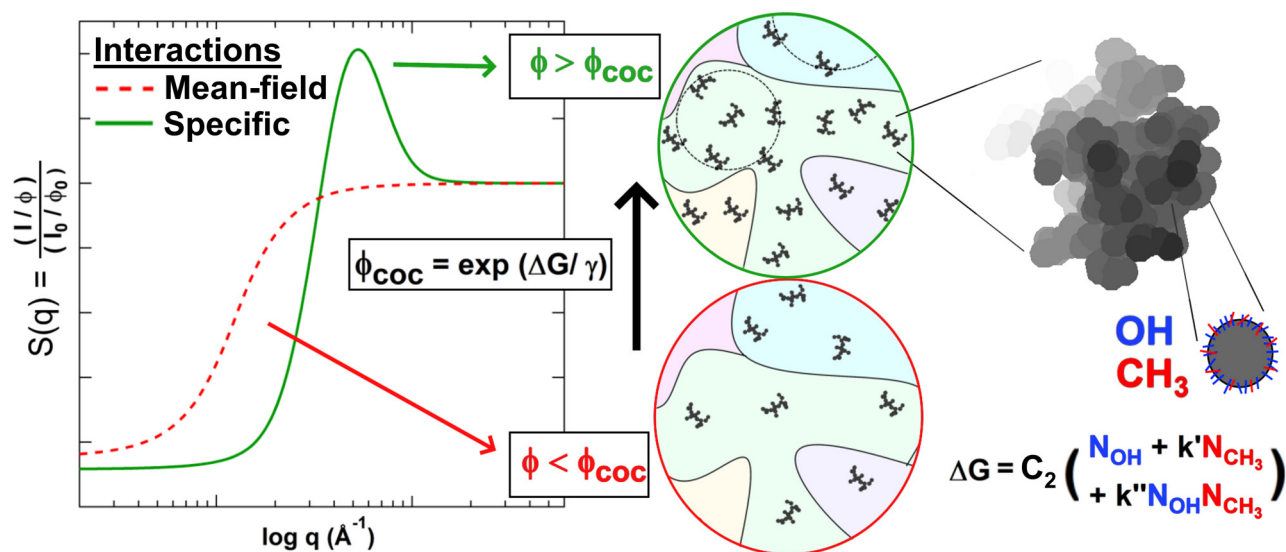
FIG. 14. Summary of the critical ordering phenomena in conventional and surface-modified fumed silica and their relative concentrations in non-polar matrices.

CONCLUSIONS

The effect of polar and non-polar surface functionalities on the dispersion of fumed silica nanofillers in various non-polar polymer matrices, viz., polystyrene, SBR, and PDMS was studied. The hydrophilic (polar) silica grades contained only hydroxy groups on the surface, whereas the treated hydrophobic (non-polar) silica grades contained both hydroxy and methyl surface groups. The surface concentration of these groups was determined using FTIR spectroscopy. Structural analysis and aggregate dispersion were quantified through USAXS. PS based nanocomposites were extruded, while SBR based and PDMS based nanocomposites were dispersed in a Brabender mixer and vortex mixer, respectively. On mixing of silica with polymer, the average size of the primary particles can increase or decrease. This is associated with the added functionality, the polymer matrix, and the accumulated strain. Aggregates also change in the degree of aggregation and in branch content after mixing with an elastomer. This behavior can be explained with simple associations related to compatibility or incompatibility as well as the fact that smaller nanoparticles more easily aggregate. The largest scale agglomerate or filler network structures also show predictable trends with surface modification such that bound polymer content increased with increased surface methyl content.

Incompatible systems comprised of fillers with a polar surface in non-polar polymers resulted in concentration dependent ordering for polymers. A critical order concentration, ϕ_{COC}, analogous to the critical micelle concentration, was observed. This was impacted by the Debye screening length, λ_D, which could be changed with the dielectric constant, κ, of the matrix polymer. A van der Waals function was used to model the second virial coefficient as a function of the accumulated strain in analogy to temperature. The accumulated strain could be calculated from the mixing

duration, mixing geometry, rotor speed, and the polymer viscosity. The van der Waals function yielded the excluded volume, which could be used to determine the bound polymer content and an energetic term that was related to the surface concentration of both hydroxyl and methyl groups. An exponential dependence of the energetic term balanced by the accumulated strain on the surface concentration of functional groups indicated that the proposed model is well behaved. It is found that the emergence of a complex multi-hierarchical structure can be tuned in an understandable and predictable way with surface chemistry, but that the resulting structural emergence is fairly complex and in some cases counterintuitive.

SUPPLEMENTARY MATERIAL

See the supplementary material for the fit parameters and calculated aggregate topological parameters for fumed silica fillers before and after dispersion in SBR, PS, and PDMS polymers; $\frac{I_0(q)}{\phi_0}$ vs q for dilute filler concentrations in PS and PDMS nanocomposites; $S(q)$ vs q for semi-dilute filler concentrations in PS and PDMS nanocomposites; rheological master curves for neat PS and SBR polymers at processing temperatures. The supplementary material also includes stereographs of the six three-dimensional structures determined from scattering in Fig. 4 as well as video files of these structures showing 3D rotation.

ACKNOWLEDGMENTS

REFERENCES

[1]K. Rishi, G. Beaucage, V. Kuppa, A. Mulderig, V. Narayanan, A. McGlasson, M. Rackaitis, and J. Ilavsky, Macromolecules **51**, 7893 (2018).

[2]K. Rishi, A. Mulderig, G. Beaucage, K. Vogtt, and H. Jiang, Langmuir **35**, 13100 (2019).

[3]K. Vogtt, G. Beaucage, K. Rishi, H. Jiang, and A. Mulderig, Phys. Rev. Res. **1**, 033081 (2019).

[4]A. McGlasson, K. Rishi, G. Beaucage, M. Chauby, V. Kuppa, J. Ilavsky, and M. Rackaitis, Macromolecules **53**, 2235 (2020).

[5]H. S. Khare and D. L. Burris, Polymer **51**, 719 (2010).

[6]T. Hashimoto, N. Amino, S. Nishitsuji, and M. Takenaka, Polym. J. **51**, 109 (2019).

[7]P. Akcora, H. Liu, S. K. Kumar, J. Moll, Y. Li, B. C. Benicewicz, L. S. Schadler, D. Acehan, A. Z. Panagiotopoulos, V. Pryamitsyn, V. Ganesan, J. Ilavsky, P. Thiyagarajan, R. H. Colby, and J. F. Douglas, Nat. Mater. **8**, 354 (2009).

[8]Y. Jin, G. Beaucage, K. Vogtt, H. Jiang, V. Kuppa, J. Kim, J. Ilavsky, M. Rackaitis, A. Mulderig, K. Rishi, and V. Narayanan, Polymer **129**, 32 (2017).

[9]G. Beaucage, J. Appl. Crystallogr. **28**, 717 (1995).

[10]G. Beaucage, Phys. Rev. E **70**, 031401 (2004).

[11]G. Beaucage, H. K. Kammler, and S. E. Pratsinis, J. Appl. Crystallogr. **37**, 523 (2004).

[12]N. Patel and S. A. Egorov, J. Chem. Phys. **121**, 4987 (2004).

[13]A. Bymaster, S. Jain, and W. G. Chapman, J. Chem. Phys. **128**, 164910 (2008).

[14]E. Ndong Mintsa, P. Germain, and S. Amokrane, Eur. Phys. J. E **38**, 1 (2015).

[15]J. S. Pedersen and C. Sommer, in Scattering Methods in Propagation of Polymer Materails (Springer Berlin Heidelberg, Berlin, 2005), pp. 70–78.

[16]K. Rishi, V. Narayanan, G. Beaucage, A. McGlasson, V. Kuppa, J. Ilavsky, and M. Rackaitis, Polymer **175**, 272 (2019).

[17]A. McGlasson, K. Rishi, G. Beaucage, V. Narayanan, M. Chauby, A. Mulderig, V. K. Kuppa, J. Ilavsky, and M. Rackaitis, Polymer **181**, 121765 (2019).

[18]J. W. Jansen, C. G. de Kruif, and A. Vrij, J. Colloid Interface Sci. **114**, 492 (1986).

[19]A. Mulderig, G. Beaucage, K. Vogtt, H. Jiang, Y. Jin, L. Clapp, and D. C. Henderson, Langmuir **33**, 14029 (2017).

[20]A. Mulderig, G. Beaucage, K. Vogtt, H. Jiang, and V. Kuppa, J. Aerosol Sci. **109**, 28 (2017).

[21]K. Vogtt, G. Beaucage, M. Weaver, and H. Jiang, Soft Matter **13**, 6068 (2017).

[22]K. Bahl and S. C. Jana, J. Appl. Polym. Sci. **131**, n/a (2014).

[23]J. Leblanc, Prog. Polym. Sci. **27**, 627 (2002).

[24]M.-J. Wang, S. Wolff, and J.-B. Donnet, Rubber Chem. Technol. **64**, 559 (1991).

[25]M.-J. Wang, S. Wolff, and J.-B. Donnet, Rubber Chem. Technol. **64**, 714 (1991).

[26]S. Wolff and M.-J. Wang, Rubber Chem. Technol. **65**, 329 (1992).

[27]M. McEwan and D. Green, Soft Matter **5**, 1705 (2009).

[28]A. Guinier and G. Fournet, Small Angle Scattering of X-Rays (John Wiley & Sons, New York, 1955).

[29]G. Beaucage, T. A. Ulibarri, E. P. Black, and D. W. Schaefer, in Hybrid Organic-Inorganic Composites: Multiple Size Scale Structures in Silica-Siloxane Composites Studied by Small-Angle Scattering, ACS Symposium Series, edited by J. E. Mark, C. Y.-C. Lee, and P. A. Bianconi (ACS, 1995), Vol. 585, pp. 97–111.

[30]K. Vogtt, G. Beaucage, M. Weaver, and H. Jiang, Langmuir **31**, 8228 (2015).

[31]I. Hassinger, X. Li, H. Zhao, H. Xu, Y. Huang, A. Prasad, L. Schadler, W. Chen, and L. Catherine Brinson, J. Mater. Sci. **51**, 4238 (2016).

[32]J. Ilavsky, F. Zhang, A. J. Allen, L. E. Levine, P. R. Jemian, and G. G. Long, Metall. Mater. Trans. A **44**, 68 (2013).

[33]J. Ilavsky, F. Zhang, R. N. Andrews, I. Kuzmenko, P. R. Jemian, L. E. Levine, and A. J. Allen, J. Appl. Crystallogr. **51**, 867 (2018).

[34]J. Ilavsky and P. R. Jemian, J. Appl. Crystallogr. **42**, 347 (2009).

[35]J. Ilavsky, J. Appl. Crystallogr. **45**, 324 (2012).

[36]R. Mueller, H. K. Kammler, K. Wegner, and S. E. Pratsinis, Langmuir **19**, 160 (2003).

[37]R. S. McDonald, J. Phys. Chem. **62**, 1168 (1958).

[38]V. Gottardi, M. Guglielmi, A. Bertoluzza, C. Fagnano, and M. A. Morelli, J. Non Cryst. Solids **63**, 71 (1984).

[39]A. Duran, C. Serna, V. Fornes, and J. M. Fernandez Navarro, J. Non Cryst. Solids **82**, 69 (1986).

[40]C. J. Brinker and G. W. Scherer, Sol–Gel Science. The Physics and Chemistry of Sol–Gel Processing (Academic Press, New York, 1990).

[41]L. Klapiszewski, T. J. Szalaty, J. Zdarta, and T. Jesionowski, Physicochem. Probl. Miner. Process. **52**, 459 (2016).

[42]D. W. Schaefer and R. S. Justice, Macromolecules **40**, 8501 (2007).

[43]H. K. Kammler, G. Beaucage, D. J. Kohls, N. Agashe, and J. Ilavsky, J. Appl. Phys. **97**, 054309 (2005).

[44]P. Debye and F. Bueche, J. Phys. Colloid Chem. **55**, 235 (1951).

[45]J. E. Mark, Polymer Data Handbook (Oxford University Press, New York, 1999).

[46]L. Karásek, B. Meissner, S. Asai, and M. Sumita, Polym. J. **28**, 121 (1996).

[47]S. Gunasekaran, R. K. Natarajan, A. Kala, and R. Jagannathan, Indian J. Pure Appl. Phys. **46**, 733 (2008), available at nopr.niscair.res.in/handle/123456789/2579.

[48]S. K. Kumar, N. Jouault, B. Benicewicz, and T. Neely, Macromolecules **46**, 3199 (2013).

[49]M. Bousmina, A. Ait-Kadi, and J. B. Faisant, J. Rheol. **43**, 415 (1999).

[50]S. Sadhu and A. K. Bhowmick, J. Polym. Sci. Part B **43**, 1854 (2005).

[51]T. G. Mezger, The Rheology Handbook: For Users of Rotational and Oscillatory Rheometers, 2nd ed. (Vincentz Network GmbH & Co KG, Hannover, 2006).

[52]W. P. Cox and E. H. Merz, J. Polym. Sci. **28**, 619 (1958).